Vibrational Mode Coupling to Ultrafast Electron Transfer in $[(CN)_5OsCNRu(NH_3)_5]^-$ Studied by Femtosecond Infrared Spectroscopy

Alexei V. Tivanski, Chengfei Wang, and Gilbert C. Walker*

Department of Chemistry, University of Pittsburgh, Pittsburgh, Pennsylvania 15260

Received: February 2, 2003; In Final Form: August 27, 2003

We report studies of the coupling of vibrational excitations to photoinduced electron transfer in a mixed-valence transition metal complex $[(CN)_5OsCNRu(NH_3)_5]^-$. Static metal−metal charge transfer (MMCT) spectra, infrared (IR) absorption spectra at different temperatures, resonance Raman spectra, and polarized light transient spectra were taken to reveal the solvent and vibrational coupling to reverse electron transfer. The measured reverse electron transfer rates are greater than 3×10^{12} s^{-1}. We observe excitations in the non-totally symmetric vibrational mode accompanying the reverse electron transfer process in both formamide (FA) and deuterium oxide (D_2O) solutions. A simulation of the spectral dynamics in FA and D_2O solutions is presented using a kinetic model for vibrational excitation and relaxation. The simulation includes the effect of solvent heating through coupling a low-frequency mode to a medium-frequency oscillator. The vibrational relaxation times of trans CN obtained from the spectral fits show faster vibration relaxation in D_2O than FA, reflecting an overlap of the IR absorption spectra of the solvent and the CN vibrations.

Introduction

Considerable progress has been made in recent years in both experimental and theoretical aspects of understanding electron transfer (ET) reactions in solution.[1−39] The coupling of vibrational and solvation dynamics to ET has been of particular interest. In these studies, mixed-valence transition metal dimers are popular for investigating the dynamics of ultrafast electron transfer. Understanding the microscopic details of these reactions has been the object of recent work by our group and others.[40−45]

Our goal is to understand how solute vibrational excitation couples to ET, and how the solvent couples to those vibrational mode changes after ET. In recent years researchers have related the ET rates with resonance Raman intensities and charge transfer absorption profiles.[46−48] There is an assumption in this approach that only totally symmetric modes can couple to reverse ET. Thus, it is worthwhile examining if this assumption is valid in mixed-valence transition metal dimers.

The chemical system reported on here is $[(CN)_5OsCNRu(NH_3)_5]^-$ (OsRu), which provides a well-defined environment in which to study the ET reaction. Optical absorption corresponds to direct electron transfer from Os to Ru. Radiationless decay from the electronic excited state(s) to the ground state results in reverse electron transfer. We are interested in studying the response of CN vibrations after reverse electron transfer. The metal−metal charge transfer (MMCT) processes can be represented as

$$[(CN)_5Os^{II}CNRu^{III}(NH_3)_5]^- \underset{\text{reverse ET}}{\overset{h\nu}{\rightleftharpoons}} [(CN)_5Os^{III}CNRu^{II}(NH_3)_5]^-$$

We utilize pulsed 800 nm light to excite the molecule to electronic excited state(s) (direct ET) and pulsed infrared light to probe the CN vibrational absorption after reverse ET in both formamide (FA) and deuterium oxide (D_2O) solutions. We combine the static spectroscopy and anisotropy data along with group theory analysis to assign the observed transient absorption features. Finally, we provide a simulation of transient spectra of OsRu in formamide and deuterium oxide in which we consider the effects of vibrational excitation and relaxation. In the simulation of transient spectra of OsRu in deuterium oxide we consider the time-dependent frequency shift of the low-frequency mode caused by the coupling between low- and high-frequency modes.

Experimental Methods

The apparatus and experimental method have been described in detail elsewhere.[49] Briefly, the time-resolved experiments were performed using femtosecond 800 nm pump pulses and mid-IR probe pulses. The 800 nm pump pulses (120 fs) are used to initiate the direct electron transfer, and the mid-IR probe pulses (200 fs) are used to detect the vibrational absorption of the CN stretch modes after reverse electron transfer. Thus, the signal recorded is the change of IR absorbance in the sample induced by pump pulses. Time-resolved infrared spectra and transient kinetic signals are obtained by varying the relative arrival time of pump and probe pulses at the sample and detecting transmitted IR pulses through a monochromator at a 10 element HgCdTe array detector. The spectral resolution of the IR probe light is 7 cm^{-1}. The 800 nm pump light is provided by a Ti:sapphire regenerative amplifier operated at 1.15 kHz. The mid-IR light is generated using optical parametric amplifier (OPA) and difference frequency generation (DFG) techniques. A β-barium borate (BBO) OPA is pumped by 800 nm pulses to generate near-IR pulses (signal and idler). Tunable mid-IR is subsequently generated in a $AgGaS_2$ crystal (1 mm path length, 39° cut for type II phase-matching) by mixing signal and idler pulses via difference frequency generation. The OPA is operated in a double-pass configuration. The first pass of the OPA in the BBO crystal (3 mm path length, 27° cut for type II phase-matching) is pumped with 800 nm light and seeded with

* Corresponding author. E-mail: gilbertw@pitt.edu.

10.1021/jp034274v CCC: $25.00
Published on Web 10/07/2003

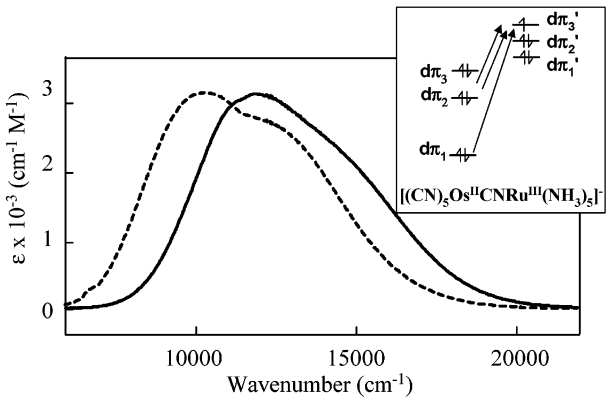

Figure 1. Metal−metal charge transfer absorption spectra of OsRu in D_2O (solid line) and formamide (dotted line). The inset shows the direct electron transfer process.

a white light continuum, which is generated by focusing a small fraction (1−5 μJ) of fundamental 800 nm light into a 4 mm thick sapphire plate. After the second pass through the BBO crystal, the signal and idler are focused into a $AgGaS_2$ crystal for difference frequency generation. Mid-IR tunable from 3 to 8 μm with 1 μJ pulse energy and 200 fs pulse width (fwhm) can be obtained.

Formamide (FA) and *N*-methyl formamide (NMF) were purchased from Aldrich and used without further purification. Deuterium oxide (D_2O) was obtained from Cambridge Isotopes. For static IR absorption and resonance Raman measurements, the concentrations of OsRu were 10^{-3} M in D_2O, FA, and NMF. These measurements were performed using FTIR and FT-Raman spectrometers (Nicolet 800). For Raman measurements, the excitation wavelength was 1064 nm obtained from a YAG laser; the laser power for these experiments was 350−400 mW. The sample was placed in a 4 mm diameter NMR tube and stirred by a magnetic stirrer to avoid localized heating of the sample by the YAG laser light.

For transient absorbance measurements, the sample solution was placed in a spinning cell with thin CaF_2 windows which provided a fresh sample volume for every laser shot (1.15 kHz). The concentrations of OsRu were 0.02 M in D_2O and 0.008 M in FA. The path length was 0.2 mm for D_2O experiments and 0.5 mm for FA experiments. The pump (800 nm) and probe (mid-IR) beams were combined and focused into the sample collinearly using a dichroic mirror. The pump and probe beams were focused to spot sizes of 0.2 and 0.15 mm in diameter, respectively. The pump energy was 3 μJ/pulse. A zero-order half-wave plate was placed in the pump beam to provide for polarization-dependent measurements.

Results

Figure 1 shows the metal−metal charge transfer (MMCT) absorption spectra of OsRu in D_2O and formamide (FA) solvents. The absorption bands are strongly solvent broadened. In this complex the available donor orbitals derive from the nominally degenerate 5dπ orbitals of the Os center. If we define the *z*-axis as lying along the two metal centers and bridging CN, then two of these orbitals (d_{xz} and d_{yz}) are directed on the *z*-axis and the third (d_{xy}) is orthogonal. In O_h symmetry, the three dπ orbitals of the metal are degenerate. Due to spin−orbit coupling and ligand-field asymmetry, they are partially split in symmetries lower than O_h into the nondegenerate dπ_1 orbital and a degenerate pair of orbitals (dπ_2 and dπ_3). The spin−orbit (SO) coupling is about 3200 cm^{-1} for osmium and

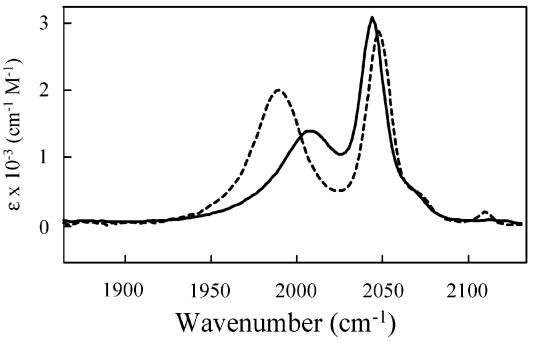

Figure 2. Infrared absorption spectra of OsRu in D_2O (solid line) and formamide (dotted line) in the CN stretch region.

TABLE 1: Properties of the MMCT Absorption Band of OsRu in Solution

solvent	ν_{max} (cm^{-1})	$\Delta\nu_{fwhm}$ (cm^{-1})	ϵ_{max} (M^{-1} cm^{-1})	H_{ab} (cm^{-1})
D_2O	11 750	8960	3010	2300
FA	10 150	7380	3020	1950

TABLE 2: Properties of CN Stretch Infrared Absorption Bands of OsRu in Solution

solvent	mode	ν_{max} (cm^{-1})	$\Delta\nu_{fwhm}$ (cm^{-1})	ϵ_{max} (M^{-1} cm^{-1})
D_2O	*bridge* CN	2115	9 ± 1	30
D_2O	*cis* CN	2045	16 ± 0.04	2760
D_2O	*trans* CN	2010	45 ± 0.2	1400
FA	*bridge* CN	2110	10 ± 0.4	130
FA	*cis* CN	2050	17 ± 0.03	2800
FA	*trans* CN	1990	34 ± 0.07	1990

1100 cm^{-1} for ruthenium.[50,51] The bandwidth in OsRu is 2100 cm^{-1} broader than in $[(CN)_5Fe^{III}CNRu^{II}(NH_3)_5]^-$ (FeRu), which is expected to have similar nuclear reorganization energy but 2000 cm^{-1} less SO coupling. The absorption measurements make possible the evaluation of nonadiabatic electronic coupling energies, H_{ab}. We have estimated the electron coupling between $Os^{II}Ru^{III}$ and $Os^{III}Ru^{II}$ states using the Hush−Mulliken analysis:[50,58]

$$H_{ab} = ((4.2 \times 10^{-4})\epsilon_{max}\Delta\nu_{FWHM}\nu_{max}/d^2)^{1/2} \qquad (1)$$

Here ϵ_{max} is the maximum of the extinction coefficient, $\Delta\nu_{fwhm}$ is the full width at half-maximum (fwhm) of the band, and ν_{max} is the center frequency of the band. The distance between the metal centers *d* is taken to be 5 Å. The properties of the MMCT band are summarized in Table 1. We conclude that the MMCT band's peak frequency, width, and H_{ab} are strongly solvent coupled.

Figure 2 shows the static infrared absorption spectra of OsRu in the CN stretch region for D_2O and formamide solvents. There are two main features in the infrared absorption spectra. There is a strong band at around 2050 cm^{-1} and a strong wide band at around 2000 cm^{-1}, which is strongly influenced by the solvent. Two weak bands are seen at ca. 2110 and 2070 cm^{-1}, respectively. The characteristics of the vibrational absorption bands in the CN stretch region are summarized in Table 2.

Figure 3 shows the resonance Raman spectra of OsRu in the CN stretch region in D_2O and formamide solvents. There is a strong band near 2110 cm^{-1}, and one wide band at around 2000 cm^{-1}. No Raman band is seen around 2050 cm^{-1}, in contrast to the infrared absorption spectra.

Figure 4 shows the time-resolved infrared difference spectra of OsRu in FA solvent with pump polarization perpendicular

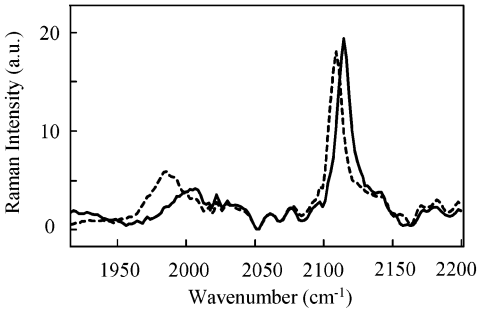

Figure 3. Resonance Raman spectra of OsRu in D_2O (solid line) and formamide (dotted line) in the CN stretch region. The excitation wavelength is 1064 nm.

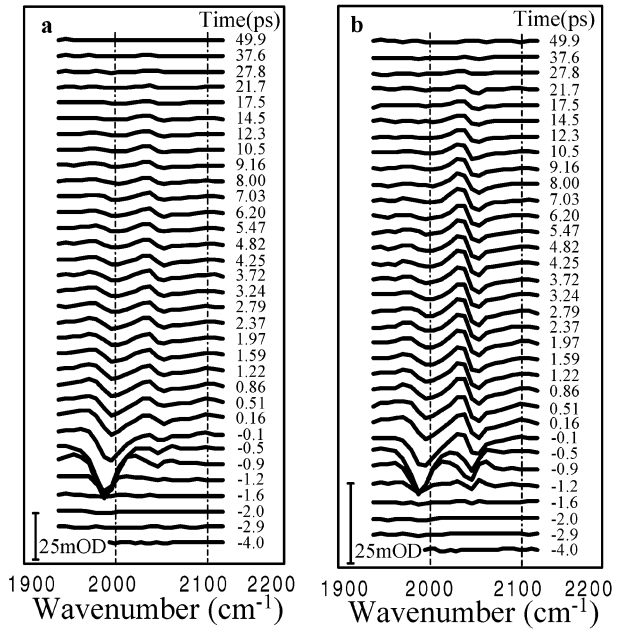

Figure 4. Transient infrared spectra of OsRu in formamide solvent. (a) The relative polarization of pump (800 nm) and probe (mid-IR) pulses is parallel. (b) The relative polarization of pump (800 nm) and probe (mid-IR) pulses is perpendicular.

and parallel to the probe polarization. Negative $-\Delta$OD features correspond to the loss of ground vibrational state absorbance due to optical excitation, and positive ΔOD features correspond to the increase of ground vibrational state absorbance or new vibrational absorption created as a result of excitation by the optical pump pulses (800 nm). At positive times, there are bleaches of ground state absorbance at ca. 2050 and 2000 cm^{-1}, respectively. The new absorption is seen at ca. 2100, 2030, and 1975 cm^{-1}.

Figure 5 shows the time-resolved infrared difference spectra of OsRu in deuterated water solvent with pump polarization perpendicular and parallel to the probe polarization, respectively. At positive times, there are bleaches of ground state absorbance at ca. 2050 and 2000 cm^{-1}, respectively. The new absorption is seen at ca. 2030 and 1995 cm^{-1}.

Figures 6 and 7 show the time-resolved visible difference spectra of OsRu in D_2O solvent with pump polarization perpendicular and parallel to the probe polarization, respectively.

Discussion

Based on the spin−orbit (SO) states picture (shown in the inset of Figure 1) there are two overlapping intervalence

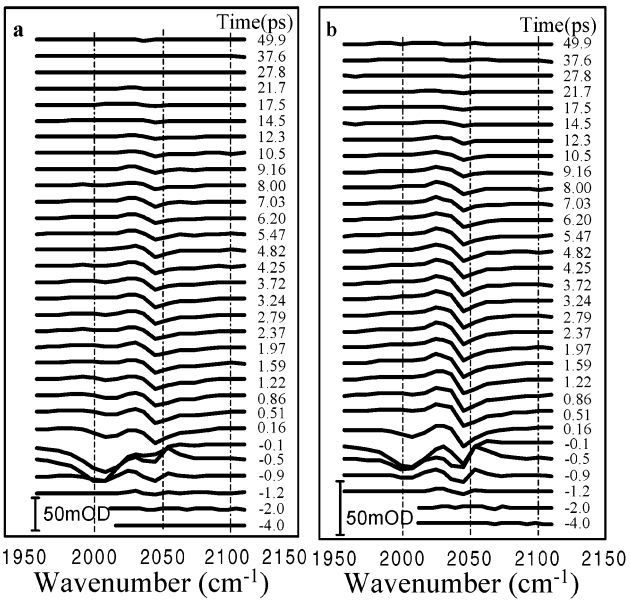

Figure 5. Transient infrared spectra of OsRu in deuterium water solvent. (a) The relative polarization of pump (800 nm) and probe (mid-IR) pulses is parallel. (b) The relative polarization of pump (800 nm) and probe (mid-IR) pulses is perpendicular.

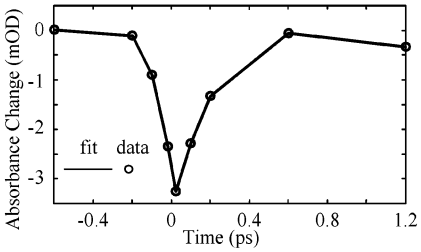

Figure 6. Transient visible difference spectra of OsRu in D_2O solvent with pump polarization (800 nm) perpendicular to the probe polarization (800 nm). The fit is based on the direct step-function extrapolation of the pulse profile. Assuming a one exponential decay process, we obtain a relaxation time of 180 fs.

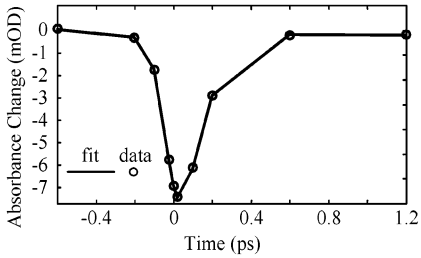

Figure 7. Transient visible difference spectra of OsRu in D_2O solvent with pump polarization (800 nm) parallel to the probe polarization (800 nm). The fit is based on the direct step-function extrapolation of the pulse profile. Assuming a one exponential decay process, we obtain a relaxation time of 140 fs.

transitions. The lower energy, high-intensity transition band is the optical intervalence electron transfer band from the degenerate pair of donor orbitals ($d\pi_2$ and $d\pi_3$). The high-energy, lower intensity transition band is an intervalence electron transfer band from the single donor orbital ($d\pi_1$).

To fit the static absorption spectra, we will use a line shape that includes a classical and a high-frequency quantal degree of freedom. The form of the line shape is therefore a sum of Gaussians in a Franck−Condon (FC) distribution (vibronic shape factor).

TABLE 3: Properties of Resonance Raman Bands of OsRu in Solutions and Calculated Normal Mode Distortion Δ with Vibrational Reorganization Energy χ_I for the Different Modes

solvent	mode	ν_{max} (cm^{-1})	$\Delta\nu_{fwhm}$ (cm^{-1})	I (au)	D	χ_I (cm^{-1})
D_2O	*bridge* CN	2115	15	19	2.5	1400
D_2O	*trans* CN	2010	55	4	1.3	330
FA	*bridge* CN	2110	15	17	2.6	1510
FA	*trans* CN	1990	40	6	1.6	570

Variations in Raman intensity I among the modes can be connected to unitless normal-coordinate distortions Δ:

$$\frac{I_1}{I_2} = \frac{\omega_1^2 \Delta_1^2}{\omega_2^2 \Delta_2^2} \tag{2}$$

The magnitudes of Δ's can in principle be determined from the width of the absorption band by using eq 3:[52,53]

$$2\sigma^2 = \sum_k \Delta_k^2 (\nu_k)^2 = \sum_k \Delta_k^2 (\omega_k/2\pi)^2 \tag{3}$$

where ω_k is 2π times the vibrational frequency ν_k and $2\sigma^2$ is the square of the absorption band at half of the height. From the normal coordinate or bond distortion data, individual contribution χ_i to the vibrational reorganization energy can be calculated:

$$\chi_i = \frac{1}{2}\Delta_i^2 \nu_i \tag{4}$$

Based on the resonance Raman spectra of OsRu in the CN stretch region in D_2O and formamide solvents (shown in Figure 3) we can assign Raman intensities and frequencies for different modes. Since $2\sigma^2 = (\Delta\nu_{1/2})^2$, where $\Delta\nu_{1/2}$ is the fwhm of the absorption spectra, we can calculate σ for different solvents. Using these data together with eqs 2−4, we can calculate normal-coordinate distortions and vibrational reorganization energy for different modes in different solvents. The results are summarized in Table 3. We note the metal−carbon stretch modes might be expected to show activity;[40] within the modest signal-to-noise ratio of the resonance Raman spectra, no such activity was observed in the expected region of the spectrum.

To fit the static absorption spectra, we use a line shape that includes a classical and one high-frequency quantal degree of freedom. The form of the line shape is therefore a sum of Gaussians in a Franck−Condon distribution (vibronic shape factor). The nuclear Franck−Condon factors for connecting $n = 0$ of the ground state and the nth vibrational state for the excited state are

$$|\langle 0|n\rangle|^2 = \frac{S^n}{n!}\exp(-S)$$

where the electron−vibrational coupling strength is $S = (\chi_i/\nu_i)$.

Since there are two modes (*trans* CN and *bridge* CN) and assuming that the absorption spectra consist of two bands, then the overall line shape becomes

$$F(\nu) \propto \sum_i \sum_m \sum_n |\langle 0|n\rangle|^2 |\langle 0|m\rangle|^2 \exp\left[-\frac{(\Delta G^0_{i,m,n} + \lambda_{cl} - h\nu)^2}{4\lambda_{cl} k_B T}\right]$$

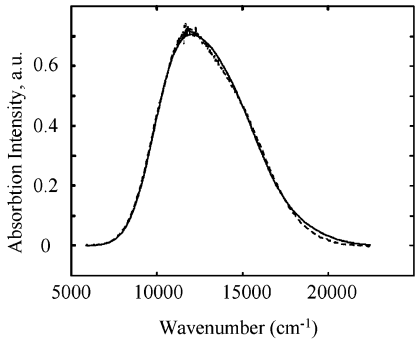

Figure 8. Fit of the OsRu absorption spectra in D_2O with a 1:2 amplitude ratio for the relative cross sections of the two characteristic spin−orbit transitions. The dashed line represents the data, while the solid line is the fit to the data.

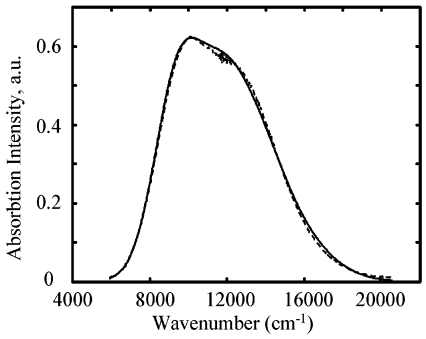

Figure 9. Fit of the OsRu absorption spectra in formamide with 1:2 amplitude ratio for the relative cross sections of the two characteristic spin−orbit transitions. The dashed line represents the data, while the solid line is the fit to the data.

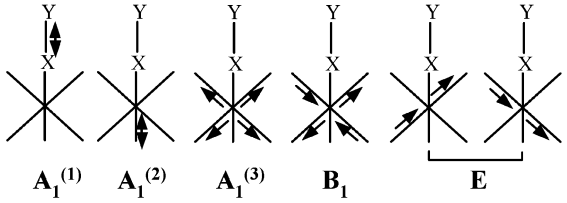

Figure 10. Vibrational normal modes of CN vibrations based on a simplified local C_{4v} symmetry of an OsRu molecule.

where the modified free energy difference, ΔG^0_i, $i = 1, 2$, is $\Delta G^0_{i,n,m} = \Delta G_i^0 + nh\nu_{trans} + mh\nu_{bridge}$ and λ_{cl} is the classical reorganization energy. In the current procedure, we will neglect terms $|\langle 0|k\rangle|^2$ for $k = 3, 4, \ldots$ since these terms becomes negligible; we will use only $k = 0, 1, 2$.

Figures 8 and 9 show a fit of the absorption spectra of OsRu in D_2O and in FA with two bands, 1:2 amplitude ratio, and the same classical reorganization energy λ_{cl} (proportional to the square of fwhm for each band). From the fitting one obtains for D_2O, $\Delta G_0^{(1)} = 12\,550$ cm^{-1}, $\Delta G_0^{(2)} = 8730$ cm^{-1}, $\lambda_{cl} = 2220$ cm^{-1}, and for FA, $\Delta G_0^{(1)} = 9750$ cm^{-1}, $\Delta G_0^{(2)} = 7610$ cm^{-1}, $\lambda_{cl} = 1670$ cm^{-1}. These results are consistent with the higher dielectric constant for D_2O than FA.

Figure 10 shows a simplified picture of the transition metal complex and the CN vibrational modes. From group theory, the total stretching CN normal modes include three A_1, one B_1, and two E modes of $(CN)_5OsXY$ in C_{4v} symmetry, where *XY* represents the bridging CN group. Or we can write $\Gamma_{stretch} = 3A_1 + B_1 + E$. IR active modes are A_1 and E, and Raman active modes are A_1 and B_1 in these stretching modes.

Through anisotropy measurements (shown in Figures 4 and 5), one can obtain the ensemble-averaged angles between

TABLE 4: Anisotropy Values of CN Modes of OsRu in Formamide

frequency (cm^{-1})	R/θ	mode assignment
2000	$0.26 \pm 0.05/29° \pm 6°$	*trans* CN
2050	$-0.2 \pm 0.04/90° \pm 15°$	*cis* CN
2030	$-0.2 \pm 0.04/90° \pm 15°$	$\upsilon = 1 \rightarrow \upsilon = 2$ *cis* CN
1970	$0.16 \pm 0.05/39° \pm 5°$	$\upsilon = 1 \rightarrow \upsilon = 2$ *trans* CN
2080	$0.05 \pm 0.02/50° \pm 10°$	
2100	$0.05 \pm 0.02/50° \pm 10°$	

electronic and vibrational transition moments using eqs 5 and 6. The anisotropy is calculated from the formula

$$r(t) = \frac{(I_{\parallel} - I_{\perp})}{(I_{\parallel} + 2I_{\perp})} \quad (5)$$

where $I_{\parallel}$ and $I_{\perp}$ are the absorption intensity changes for the probe IR beam polarized parallel and perpendicular to the optical excitation pulse, respectively.

The angle between the electronic transition moment and the vibrational transition moment can be calculated as

$$\langle \cos^2(\theta(t)) \rangle = (1 + 5r(t))/3 \quad (6)$$

From this measurement, the bands at 2050 and 2030 cm^{-1} are found to be close to perpendicular to the electronic transition moment, and the bands at 2000 and 1970 cm^{-1} are close to parallel to the electronic transition moment. The anisotropy values are listed in Table 4.

Hester and Swanson found that the highest frequency CN stretch mode in binuclear complexes was the bridging CN mode.[54,55] Thus the 2110 cm^{-1} mode is assigned here as the *bridge* CN ($A_1^{(1)}$) mode. Considering that the 2000 cm^{-1} stretch mode is close to parallel to the electronic transition moment, we can assign the mode at 2000 cm^{-1} as the *trans* CN ($A_1^{(2)}$) mode. Because the 2050 cm^{-1} stretch mode is perpendicular to the electronic transition moment and it is IR active, it must be $A_1^{(3)}$ or E. Since the $A_1^{(3)}$ mode is the totally symmetric stretching of the *cis* CN group, the E mode should have greater IR intensity. Therefore the 2050 cm^{-1} band is assigned here as the *cis* CN (E). Here *cis* means *cis* to the bridge and *trans* means *trans* to the bridge. Considering anharmonicity, the absorption at 2030 cm^{-1} is assigned here as $\upsilon = 1 \rightarrow \upsilon = 2$ absorption of *cis* CN. Similarly, the absorption at 1975 cm^{-1} is assigned as the $\upsilon = 1 \rightarrow \upsilon = 2$ absorption of *trans* CN.

Simulation of the Observed Dynamics. We have developed in a previous publication[41] an analytical method to simulate the observed spectral dynamics. In this simulation we assume that the vibrational state distribution is generated in the radiationless decay process. The simulation considers the cross section and population dynamics of the *cis*, *trans*, and *bridge* modes after electron transfer. The following equations were used to calculate the vibrational populations:

$$dF_{j,i}(t)/dt = K_{j,i+1}F_{j,i+1}(t) - K_{j,i}F_{j,i}(t) \quad (7)$$

$$\sum_{i=0}^{k} F_{j,i}(t) = \sum_{i=0}^{k} F_{j,i}(0) \quad (8)$$

$$K_{j,k+1} = K_{j,0} = 0 \quad (9)$$

where i ($i = k, k-1, ..., 0$) denotes vibrational states and j ($j = 1, 2$) corresponds to *trans* and *cis* modes; $K_{j,i}$ is the rate constant. $F_{j,i}(t)$ is the population of vibrational state i at time t and $F_{j,i}(0)$ is the initial population of state i. From the harmonic oscillator approximation, $K_{j,i} = iK_{j,1}$, and this can be used to estimate the vibrational state-dependent cross section.

Including the effects of vibrational anharmonicity[56] and a Gaussian line shape for each vibrational resonance, the transient ΔOD signal (after reverse ET) is

$$\Delta A(t,\nu) = \sum_{i=0}^{k} c_i(i+1)B_{1,i}(t,\nu)[F_{1,i}(t) - F_{1,i+1}(t)] - c_1B'_{1,0}(\nu) + \sum_{i=0}^{k} c_2(i+1)B_{2,i}(t,\nu)[F_{2,i}(t) - F_{2,i+1}(t)] - c_2B'_{2,0}(\nu) + c_3B_{3,0}(\nu)F_{3,0}(t)c_4B_{4,0}(\nu)F_{4,0}(t) \quad (10)$$

Here ΔA is the induced absorbance change and c_1, c_2, c_3, and c_4 are cross section scaling factors. $B_{1,i}(t,\nu)$ and $B_{2,i}(t,\nu)$ are the Gaussian line shape functions with time-dependent amplitudes ($i = 0-k$, corresponding to different vibrational states). $B'_{1,0}(\nu)$, $B'_{2,0}(\nu)$, $B_{3,0}(\nu)$, and $B_{4,0}(\nu)$ are the Gaussian line shape functions of the modes in the ground vibrational state. $F_{1,i}(t)$ and $F_{2,i}(t)$ are the populations of vibrational state i at time t for modes 1 and 2. $F_{3,0}(t)$ and $F_{4,0}(t)$ have the form of an exponential decay. The Gaussian line shape function is

$$B_{j,i}(t,\nu) = (1 + f\exp(-t/\tau))\exp(-(\nu - \nu_{j,0})^2/w_{j,0}^2) \quad (11)$$

where $\nu_{j,0}$ is the band center frequency, which might be time-dependent as will be shown below, and $w_{j,0}$ is its width. f is a parameter that accounts for the temperature dependence of the cross section; it is zero for the unpumped state. τ is the time constant for the time dependence of the cross section due to solvent cooling.

For these high-frequency vibration modes, the Boltzman factors place essentially all of the population in the $\upsilon = 0$ state (the ground state) at negative times. At positive times, non-equilibrium vibrational populations are generated by optical excitation and reverse electron transfer. The $B_{j,i}(t,\nu)F_{j,i}(t)$ term represents the stimulated absorption from vibrational state i, and the $B_{j,i}(t,\nu)F_{j,i+1}(t)$ term represents stimulated emission from state $(i+1)$ to i. The $B_{3,0}(\nu)F_{3,0}(t)$ term corresponds to the absorption due to the cross section increase as the temperature increases. The $(i+1)$ term in eq 10 comes from the vibrational excited state dependence of the vibrational transition cross section; within the harmonic oscillator approximation, μ_i^2 is proportional to $(i+1)$, where μ^2 is proportional to the absorption cross section. The results show that vibrational levels $\upsilon = 0$, $\upsilon = 1$, and $\upsilon = 2$ of *cis* and *trans* CN are populated after reverse ET. The fitted spectra for OsRu in FA are shown in Figure 11. The fitted parameters are listed in Table 5.

The fitted initial populations show vibrational excitation of IR active modes that are not present in the resonance Raman data in Table 3. We do not know the mechanism that leads to the observed distribution. The initially prepared electronic state has excitation in the totally symmetric modes of the system. Energy could be deposited in the IR active modes via evolution of the geometry of the molecule in the excited state or a vibration of suitable symmetry could couple the totally symmetric mode with the IR active mode in a fast relaxation process.[57] We note that the spin−orbit states of the t_{2g} manifold are quite close, and relaxation within them may occur on the time scale of the observed dynamics.

The time-resolved visible difference spectra of the OsRu in D_2O solvent with pump polarization perpendicular and parallel to the probe polarization, respectively, were collected (see

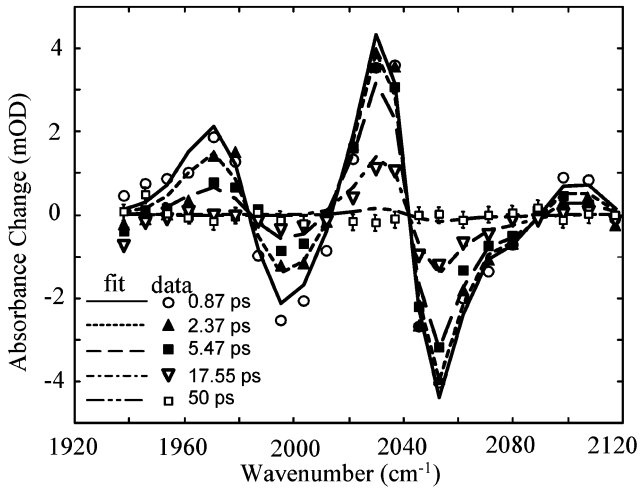

Figure 11. Actual and simulated pump probe difference spectra of OsRu in formamide. Open circles correspond to 0.87 ps delay data (solid line is simulation); solid triangles correspond to 2.37 ps delay data (dotted line is simulation); solid squares correspond to 5.47 ps delay data (dashed line is simulation); open triangles correspond to 17.55 ps data (dash dot line is simulation); open squares correspond to 50 ps delay data (dash double dot line is simulation).

TABLE 5: Fit Parameters for OsRu Reverse Electron Transfer Kinetics in Formamide

	initial vibrational populations via reverse ET ($F_{j,i}(0)$)			
mode	$v = 0$	$v = 1$	$v = 2$	$T_{j,1}$ (ps) ($1/K_{j,1}$)
trans CN	0.63 ± 0.1	0.34 ± 0.07	0.03 ± 0.01	3.6 ± 0.5
cis CN	0.75 ± 0.1	0.25 ± 0.05	0.00 ± 0.02	15 ± 2

Figures 6 and 7). The shown fit was based on the direct step-function extrapolation of the pulse profile. Assuming a single-exponential decay, the relaxation time is 180 fs for pump pulse polarization perpendicular to the probe pulse polarization and 140 fs for pump pulse polarization parallel to the probe pulse polarization. Other researchers have found that electronic relaxation time within spin−orbit states in a similar transition metal complex is on the time scale of 100 fs.[58] Additional experiments that examine electronic transitions between spin−orbit states of Os^{III} should be done in the future to better address the role of spin−orbit relaxation.

Model for Low-Frequency Mode Coupling. In contrast with the time-resolved OsRu data in formamide, OsRu data in D_2O are not well-fit by the model described above; the low-frequency portion of the induced IR absorption shows a time-dependent frequency shift that the above model does not describe. A possible explanation is the effect of bath (solvent) heating through coupling a low-frequency oscillator to a medium-frequency oscillator. This could be a suitable representation of specific, albeit weak, hydrogen bonding of a nitrile ligand to the solvent bath. Others have shown that anharmonic coupling of low-frequency modes to a medium-frequency mode leads to a temperature-dependent shift in the IR transition frequency and broadening of the resonance band.[3,58] We represent the anharmonic potential of the *trans* CN stretch mode coordinate, *X*, and the intermolecular bond coordinate, *x*, as a Taylor series in the displacements. As was shown by Cornelius[59] and Hochstrasser,[3] the dominant anharmonic contribution in the series expansion is the term proportional to $\varphi x^2 X^2$, where φ is the coupling constant. The equation of motion may be solved under the Born−Oppenheimer approximation where the *trans* CN stretch motion at high frequency may be solved for a fixed position of the low-frequency mode. If $2\varphi x^2 \ll M\Omega^2$, where *M* and Ω are the reduced mass and frequency of the *trans* CN mode, respectively, then the transition frequency for the transition from the lowest to the first excited state of the *trans* CN stretching mode is $\Omega(x) = \Omega_{1'1} + \xi x^2$, where $\xi \equiv \varphi/M\Omega$.

The frequency of the low-frequency mode is assumed to be less than *kT*, and the mode's equation of motion, if coupled to a solvent bath, may be represented by a Langevin equation.[3] In the overdamped limit, when the friction γ exerted by the bath on the low-frequency oscillator is larger than the oscillator frequency ω, the dynamics are governed by the parameter $\lambda \equiv \omega^2/2\gamma$. Solution of the Langevin equation in the overdamped limit leads to the frequency of the *trans* CN stretch.

$$\Omega_{1'1}(t,T) = \Omega_{1'1} + \xi \frac{2\lambda k_B}{m\omega^2} \int_{-\infty}^{t} \mathrm{d}t' T(t') e^{-2\lambda(t-t')} \qquad (12)$$

Here $T(t)$ is an instantaneous bath temperature due to radiationless decay. When the low-frequency oscillator is strongly overdamped, the *trans* CN transition frequency becomes linearly proportional to the bath temperature, as the bath and oscillator are in continuous equilibrium.

There is considerable local heating as a consequence of energy release of the radiationless decay process (ca. 12 000 cm^{-1}). In our case the origin of temperature/time dependence is due to local solvent/solution cooling. It was shown[41] that temperature as a function of time can be fit as a exponential decay ($\tau \approx 1-2$ ps time constant). Using this assumption, the integral in eq 12 can be calculated directly and eq 12 can be simplified to

$$\Omega_{1'1}(T,t) = \Omega_{1'1} + \frac{\varphi}{M\Omega} \frac{k_B T(t)}{m\omega^2} = \Omega_{1'1} + \frac{\varphi}{M\Omega} \frac{k_B \Delta T(0) \exp\left(-\frac{t}{\tau}\right)}{m\omega^2}$$

To find $\Delta T(0)$, we need to calculate the magnitude of the temperature increase of the surrounding water molecules caused by radiationless decay of 12 000 cm^{-1}. If we roughly estimate the "heating" volume of the water molecules to include only the first solvation shell with size 6 Å × 6 Å × 10 Å and assume the bulk H_2O heat capacity applies, then $\Delta T(0) \cong 100$ K.

We can now apply this model to simulate the transient difference spectra for OsRu in deuterium water. We add a time-dependent frequency shift $\Omega_{1'1}(T,t) - \Omega_{1'1}$ which is proportional to the temperature and time-dependent bandwidth for the *trans* CN mode. The simulated spectra are shown in Figure 12. From the simulation, we find that after reverse ET, vibrational levels $v = 0$, $v = 1$, and $v = 2$ of *cis* and *trans* CN are populated. The results are summarized in Table 6. From the fit, the time constant for the temperature exponential decay process is 1.3 ps, which is in good agreement with our previously reported results for a related mixed-valence compound[41] and several times faster than is characteristic of bulk thermal conductivity of water. The importance of including the solvent heating effect is shown for the *trans* CN stretch region in the inset of Figure 12. We note that the vibrational relaxation times of *trans* CN obtained from the fit show faster vibrational relaxation in D_2O than in FA.

To understand why formamide, a very strong hydrogen bonding solvent, does not show a time-dependent frequency shift in transient difference spectra, static infrared absorption spectra in the CN stretch region in D_2O, formamide, and *N*-methyl formamide (NMF) at 25 and 90 °C were collected (see Figures 2, 13, and 14). From the spectra at 25 °C, the *trans* CN mode

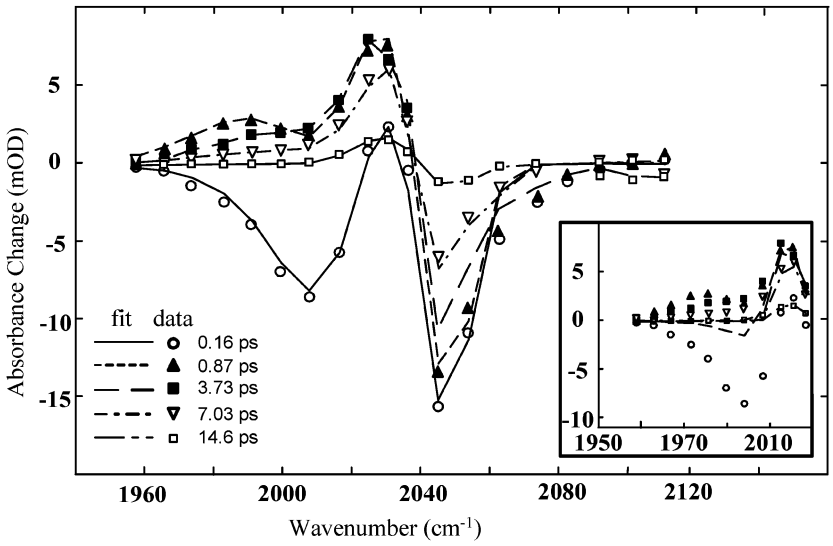

Figure 12. Actual and simulated pump probe difference infrared spectra of OsRu in deuterium water. Open circles correspond to 0.16 ps delay data (solid line is the simulation); solid triangles correspond to 0.87 ps delay data (dotted line is the simulation); solid squares correspond to 3.73 ps delay data (dashed line is simulation); open triangles correspond to 7.03 ps data (dash dot line is the simulation); open squares correspond to 14.6 ps delay data (dash double dot line is the simulation). Inset shows that a model without solvent heating cannot describe the observed kinetics for the *trans* CN stretch region. The inset shows fit results for OsRu at D_2O without solvent heating; the lines are the simulated data.

TABLE 6: Fit Parameters for OsRu Reverse Electron Transfer Kinetics in Deuterium Water[a]

	initial vibrational populations via reverse ET ($F_{j,i}(0)$)			
mode	$v = 0$	$v = 1$	$v = 2$	$T_{j,1}$ (ps)
trans CN	71 ± 5%	23 ± 5%	6 ± 1%	0.81 ± 0.1
cis CN	75 ± 6%	21 ± 5%	4 ± 1%	3.2 ± 0.3

[a] K_1 (ps^{-1}), the time constant for the temperature exponential decay process, is 1.33.

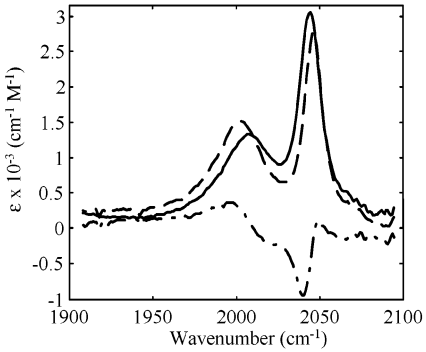

Figure 13. Infrared absorption spectra in the CN stretch region of OsRu in D_2O at 25 °C (solid line) and 90 °C (dashed line) and the difference between them (dash dot line).

shows very strong solvent (hydrogen bond) coupling in D_2O relative to the smaller coupling for FA and NMF. Static absorption IR spectra of OsRu in D_2O in Figure 13 show a *trans* CN band shift of approximately 9 cm^{-1} for a 65 °C temperature difference. In contrast, the static temperature-dependent absorption difference data in formamide (see Figure 14) show a frequency shift of approximately 4 cm^{-1}. Very significant overlap between the OsRu IR absorption band and the D_2O IR absorption cross section could provide more efficient energy transfer to the D_2O compared with formamide, where the overlap is much smaller. This might explain why the vibrational relaxation times of *trans* CN obtained from the fit show faster vibration relaxation in D_2O than in FA. Similar effects have been reported previously for the cyanide ion in H_2O and D_2O by Hochstrasser and co-workers[60] and in a related SCN^-/OCN^-

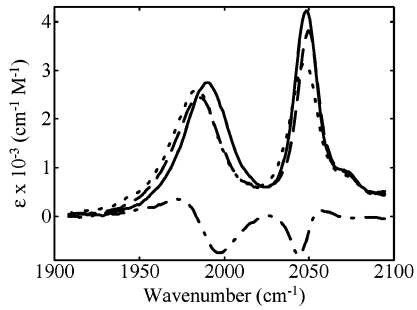

Figure 14. Infrared absorption spectra in the CN stretch region of OsRu in formamide at 25 °C (solid line) and 90 °C (dashed line), the difference spectra between them (dash dot line), and in *N*-methyl formamide at 25 °C (dotted line).

comparison in methanol by Tominaga and co-workers.[61] The smaller temperature-dependent frequency shift in FA explains why the time-resolved data in FA do not show a time-dependent frequency shift in transient difference spectra as in D_2O.

It is worthwhile to compare the magnitudes of the frequency shifts of the transient difference and static IR spectra. The maximum frequency shift of the *trans* CN band in transient difference spectra is approximately 15 cm^{-1} in D_2O for the solvent temperature change $\Delta T \approx 100$ °C. We see a shift in the static temperature-dependent absorption difference data of approximately 14 cm^{-1}, suggesting that the short-lived local heating is of a comparable 100 °C magnitude.

Summary

We have presented the time-resolved infrared spectra of $[(CN)_5Os^{II}CNRu^{III}(NH_3)_5]^-$ in formamide and deuterium water solutions following optical excitation and reverse electron transfer. The measured reverse electron transfer rates are greater than 3×10^{12} s^{-1}. We observe excitations in the non-totally symmetric vibrational mode accompanying the reverse electron transfer process in both formamide (FA) and deuterium oxide (D_2O) solutions. Transient infrared absorption spectra showed that the non-totally symmetric vibrational mode is populated after reverse ET. However, no vibrations are highly excited. We have obtained from the spectral fits the vibrational relaxation

times of *trans* CN in D_2O and FA. Our fitted results show faster vibration relaxation in D_2O than FA, reflecting a correlation of the IR absorption cross section of the solvent with the vibrational spectra of the CN. We have provided a simulation of the spectral dynamics in formamide and deuterium water solutions. In this simulation we included effects of vibrational excitation and relaxation together with effects of the coupling between the high-frequency stretch CN mode and low-frequency solvent modes, which accounts for the major components in the data. The results are similar to previous results for FeRu.

Acknowledgment. We are thankful to the Hupp research group at Northwestern University for providing the OsRu sample used in these experiments. We gratefully acknowledge the Office of Naval Research (N0001-02-D327), NSF (CHE 9816820 and PHYS 0103048), and NATO. We thank an anonymous reviewer for helpful comments.

References and Notes

(1) Stratt, R. M. *J. Phys. Chem*. **1996**, *100*, 12981.
(2) Eisenthal, K. G. *J. Phys. Chem*. **1996**, *100*, 12997.
(3) Voth, G. A.; Hochstrasser, R. M. *J. Phys. Chem*. **1996**, *100*, 13034.
(4) Barbara, P. F.; Meyer, T. J.; Ratner, M. A. *J. Phys. Chem*. **1996**, *100*, 13148.
(5) Zusman, L. D. *J. Chem. Phys*. **1980**, *49*, 295.
(6) Calef, D. F.; Wolynes, P. G. *J. Phys. Chem*. **1983**, *87*, 3387.
(7) Sparglione, M.; Mukamel, S. *J. Chem. Phys.* **1988**, *88*, 3265.
(8) Van der Zwan, G.; Hynes, J. T. *J. Chem. Phys.* **1982**, *76*, 2993.
(9) Sumi, H.; Marcus, R. A. *J. Chem. Phys.* **1986,** *84*, 4894.
(10) Marcus, R. A.; Sutin, N. *Biochim. Biophys. Acta* **1985**, *811*, 265.
(11) Marcus, R. A. *J. Chem. Phys*. **1956**, *24*, 966.
(12) Newton, M. D.; Sutin, N. *Annu. Rev. Phys. Chem*. **1984**, *35*, 437.
(13) Hwang, J. K.; Creighton, S.; King, G.; Whitney, D.; Warshel, A. *J. Chem. Phys.* **1988**, *89*, 859.
(14) Bixon, M.; Jortner, J. *Chem. Phys*. **1993**, *176*, 467.
(15) Jortner J.; Bixon, M. *J. Chem. Phys*. **1988**, *88*, 167.
(16) Bader, J. S.; Kuharski, R. A.; Chandler, D. *J. Chem. Phys.* **1990**, *93*, 230.
(17) Coalson, R. D.; Evans, D. G.; Nitzan, A. *J. Chem. Phys.* **1994**, *101*, 436.
(18) Myers, A. B. *Chem. Phys.* **1994**, *180*, 215.
(19) Myers, A. B. *Chem. Rev.* **1996**, *96*, 911.
(20) Maroncelli, M.; Fleming, G. R. *J. Chem. Phys.* **1987**, *86*, 6221.
(21) Nagasawa, Y.; Yartsev, A. P.; Tominaga, K.; Bisht, P. B.; Johnson, A. E.; Yoshihara, K. *J. Phys. Chem*. **1995**, *99*, 653.
(22) Wynne, K.; Galli, C.; Hochstrasser, R. M. *J. Chem. Phys*. **1994**, *100*, 4797.
(23) Walker, G. C.; Barbara, P. F.; Doorn, S. K.; Dong, Y.; Hupp, J. T. *J. Phys. Chem*. **1991**, *95*, 5712.
(24) Asahi, T.; Mataga, N. *J. Phys. Chem*. **1992**, *93*, 6575.
(25) Gould, I. R.; Young, R. H.; Moody, R. E.; Farid, S. *J. Chem. Phys*. **1991**, *95*, 2068.
(26) Kosower, E. M.; Huppert, D. *Annu. Rev. Phys. Chem*. **1986**, *37*, 127.
(27) Weaver, M. J.; McManis, G. E., III. *Acc. Chem. Res.* **1990**, *23*, 294.
(28) Simon, J. D.; Doolen, R. *J. Am. Chem. Soc*. **1992**, *114*, 4861.
(29) Lippert, E.; Rettig, W.; Bonacic-Koutecky, V.; Heisel, F.; Miehe, J. A. *Adv. Chem. Phys.* **1990**, *92*, 7241.
(30) Nocek, J. M.; Zhou, J. S.; DeForest, S.; Priyadarshy, S.; Beratan, D. N.; Onuchic, J. N.; Hoffman, B. M. *Chem. Rev.* **1996**, *96*, 2459.
(31) Barbara, P. F.; Jarzeba, W. *Adv. Photochem*. **1990**, *15*, 1.
(32) Maroncelli, M.; MacInnis, J.; Fleming, G. *Science* **1989**, *243*, 1674.
(33) Oxtoby, D. W. *Annu. Rev. Phys. Chem.* **1981**, *32*, 77.
(34) Simon, J. D.; Su, S. G. *Chem. Phys.* **1991**, *152*, 143.
(35) Reid, P. J.; Silva, C.; Barbara, P. F.; Karki, L.; Hupp, J. T. *J. Phys. Chem*. **1995**, *99*, 2609.
(36) Simon, J. D. *Acc. Chem. Res*. **1988**, *21*, 128.
(37) Bagchi, B. *Annu. Rev. Phys. Chem.* **1989**, *40*, 115.
(38) Maroncelli, M.; Fleming, G. *J. Chem. Phys.* **1988**, *89*, 5044.
(39) Grampp, G.; Harrer, W.; Hetz, G. *Phys. Chem.* **1990**, *94*, 1343.
(40) Wang, C.; Mohney, B. K.; Williams, R. D.; Petrov, V.; Hupp, J. T.; Walker, G. C. *J. Am. Chem. Soc.* **1998**, *120*, 5849.
(41) Wang, C.; Mohney, B. K.; Akheremitchev, B. B.; Walker, G. C. *J. Phys. Chem. A* **2000**, *104*, 4314.
(42) Stratt, R. M. *J. Phys. Chem*. **1996**, *100*, 12981.
(43) Eisenthal, K. G. *J. Phys. Chem*. **1996**, *100*, 12997.
(44) Voth, G. A.; Hochstrasser, R. M. *J. Phys. Chem*. **1996**, *100*, 13034.
(45) Barbara, P. F.; Meyer, T. J.; Ratner, M. A. *J. Phys. Chem*. **1996**, *100*, 13148.
(46) Myers, A. B. *Chem. Phys*. **1994**, *180*, 215.
(47) Myers, A. B. *Chem. Rev.* **1996**, *96*, 911.
(48) Walker, G. C.; Barbara, P. F.; Doorn, S. K.; Dong, Y.; Hupp, J. T. *J. Phys. Chem*. **1991**, *95*, 5712.
(49) Akhremitchev, B.; Wang, C.; Walker, G. C. *Rev. Sci. Instrum.* **1996**, *67*, 3799.
(50) Hupp, J. T.; Meyer, T. J. *Inorg. Chem*. **1987,** 2332.
(51) Kober, E. D.; Goldsby, K. A.; Narayana, D. N. S.; Meyer, T. J. *J. Am. Chem. Soc.* **1983**, *105*, 4303.
(52) Zink, J. I. *Coord. Chem. Rev*. **1985**, *64*, 93.
(53) Heller, E. J.; Sunberg, R. L.; Tannor, D. J. *J. Phys. Chem.* **1982**, *86*, 1822.
(54) Hester, R. E.; Nour, E. M. *J. Chem. Soc., Dalton Trans.* **1981**, 939.
(55) Swanson, B. I. *Inorg. Chem.* **1976**, *15*, 253.
(56) The vibrational anharmonicity of the CN stretch is taken to be 22 cm^{-1} in our case, as shown in: Durand, D.; Carmo, L. C. S.; Luty, F. *Phys. Rev. B* **1989**, *39*, 6096.
(57) Marin, T. W.; Homoelle, B. J.; Spears, K. G. *J. Phys. Chem. A* **2002**, *106*, 1152.
(58) Yeh, A. T.; Shank C. V.; McCusker, J. K. *Science* **2000**, *289*, 935.
(59) Shelby, R. M.; Harris, C. B.; Cornelius, P. A. *J. Chem. Phys*. **1979**, *70*, 34.
(60) Hamm, P.; Lim, M.; Hochstrasser, R. M. *J. Chem. Phys.* **1997**, *107*, 10523.
(61) Ohta, K.; Maekawa, H.; Saito, S.; Tominaga, K. *J. Phys. Chem. A* **2003**, *107*, 5643.